Λ-enhanced gray molasses in a tetrahedral laser beam geometry

D. S. Barker,[1,2] E. B. Norrgard,[1] N. N. Klimov,[1] J. A. Fedchak,[1] J. Scherschligt,[1] and S. Eckel[1,3]

[1] *Sensor Science Division, National Institute of Standards and Technology, Gaithersburg, MD 20899, USA*
[2] daniel.barker@nist.gov
[3] stephen.eckel@nist.gov

Abstract: We report observation of sub-Doppler cooling of lithium using an irregular-tetrahedral laser beam arrangement, which is produced by a nanofabricated diffraction grating. We are able to capture 11(2) % of the lithium atoms from a grating magneto-optical trap into Λ-enhanced D_1 gray molasses. The molasses cools the captured atoms to a radial temperature of 60(9) μK and an axial temperature of 23(3) μK. In contrast to results from conventional counterpropagating beam configurations, we do not observe cooling when our optical fields are detuned from Raman resonance. An optical Bloch equation simulation of the cooling dynamics agrees with our data. Our results show that grating magneto-optical traps can serve as a robust source of cold atoms for tweezer-array and atom-chip experiments, even when the atomic species is not amenable to sub-Doppler cooling in bright optical molasses.

1. Introduction

There is a large and growing effort to produce deployable quantum sensors based on laser-cooled atoms [1, 2]. An important step toward the goal of fieldable atomic sensors is miniaturizing the mainstay of laser-cooling experiments: the magneto-optical trap (MOT). One promising approach to MOT miniaturization is the grating MOT, which replaces most of the magneto-optical trap's expansive optical layout with a compact set of diffraction gratings [3, 4]. Grating MOTs are being integrated into a variety of quantum instruments and sensors, including atomic clocks [5], atom interferometers [6], electron-beam sources [7], magnetometers [8], and vacuum gauges [8, 9]. Both the diffraction gratings [10, 11] and beam launch optics [12] of a grating MOT are amenable to nanofabrication. Grating MOTs have also been integrated with compact vacuum systems [13, 14]. Chip-scale quantum sensors appear attainable in the near future on the grating MOT platform.

The simplicity of the grating MOT optics comes at the expense of decreased symmetry [15]. In a conventional six-beam MOT, formed using three orthogonal pairs of counterpropagating laser beams, the trapping forces are anti-symmetric under inversion. Thus, many properties, such as trapping forces and equilibrium temperature, are relatively easy to compute at first order by considering three nearly-identical, anti-symmetric, one-dimensional traps. By contrast, a grating MOT is formed using four or more non-orthogonal laser beams [3], and correct predictions of trapping properties are only possible by considering the full geometry of the trap [16, 17]. Sub-Doppler cooling in optical molasses becomes particularly complicated because the polarization and intensity gradients arising from the grating beam geometry do not map onto either of the standard lin⊥lin or $\sigma^+\sigma^-$ polarization gradient cooling mechanisms [18–21].

Nevertheless, sub-Doppler temperatures have been produced with tetrahedral grating beam configurations in bright optical molasses [8, 10, 21] ('bright' refers to an $F \rightarrow F' = F + 1$ transition [22], where F (F') is the total angular momentum quantum number of the ground (excited) state). Bright optical molasses is a powerful cooling method and it is a key component of atomic quantum sensors such as clocks [5] and interferometers [23, 24]. However, bright molasses is not applicable to all laser-coolable systems as it requires resolved hyperfine structure. Bright

molasses is also not ideal for certain applications, such as loading optical tweezer arrays [25].

As grating MOTs are integrated into more quantum sensors and employed to cool more species [4, 26], sub-Doppler cooling methods beyond bright optical molasses must be brought to bear. Two such methods are gray molasses [22, 27, 28] and Λ-enhanced cooling [29–31]. Both methods exploit dark states that appear in $F \geq F'$ transitions and three-level Λ-systems, respectively, to combine velocity-selective coherent population trapping (VSCPT) with polarization gradient cooling [28, 29, 31, 32]. When the cooling light is blue-detuned from the atomic transition, bright states within the ground state manifold are optically pumped into lower energy dark states. High-velocity atoms in a dark state can non-adiabatically transfer back to a bright state for further cooling, but low-velocity atoms become trapped in the dark state, yielding sub-Doppler temperatures. For systems with multiple resolved ground-state hyperfine manifolds, Λ-enhanced cooling and gray molasses can be combined to reach even lower temperatures [33, 34]. Λ-enhanced gray molasses has three main advantages over bright optical molasses. First, it is more widely applicable since many atomic and molecular species have well-resolved $F \geq F'$ transitions [33, 35]. For laser cooled and trapped molecules, Λ-enhanced cooling has emerged as the standard technique for cooling from $T \simeq 1$ mK to $T \simeq 10$ μK [35–37]. Second, it shelves atoms in dark states, greatly reducing secondary photon scattering within the atom cloud. The resulting high atom densities are essential for devices [38], such as quantum memories and single-photon sources [39], that rely on strong light-matter coupling. Third, it uses blue-detuned light, which induces light-assisted collisions that allow high efficiency loading of optical tweezer arrays [25, 40]. Although gray molasses has been studied in four-beam configurations [22], to our knowledge, neither it nor Λ-enhanced cooling have been implemented in tetrahedral or pyramidal laser beam geometries.

We report our observation of Λ-enhanced sub-Doppler cooling in an irregular-tetrahedral gray molasses produced using a nanofabricated diffraction grating. Lithium atoms are precooled in a grating MOT and subsequently transferred into a gray optical molasses operating on the lithium D_1 line. The gray molasses captures approximately 10 % of the lithium atoms from the MOT and cools them to average temperatures as low as 50 μK, well below the Doppler temperature $T_D \approx 140$ μK for lithium. Curiously, we do not see incoherent gray molasses cooling when we detune the molasses from Raman resonance [34]. To understand the low capture efficiency and lack of incoherent gray molasses cooling, we simulate the three-dimensional molasses cooling process with the optical Bloch equations. The simulations suggest that both the capture efficiency and absence of incoherent cooling are features of our experimental procedure, and not of the grating laser beam geometry. We expect that the capture efficiency could be increased to greater than 50 % using either deeper precooling or higher molasses intensity. Our results show that sub-Doppler cooling methods beyond bright optical molasses can operate in the nonorthogonal beam geometries of grating MOTs.

2. Apparatus

Our experiments take place within the grating MOT apparatus described in Ref. [4]. Additional technical information about certain aspects of our setup can be found in Refs. [41–44]. The apparatus has four principal coaxial components: a set of electromagnets, a nanofabricated diffraction grating chip, an input laser beam, and an effusive Li dispenser. The common axis of the components defines the axial unit vector $\hat{z}$. The electromagnets create a quadrupole magnetic field in front of the grating chip and continuously deform that field toward the square-root profile of a Zeeman slower behind the chip [45]. The diffraction grating chip has three linear diffraction gratings, which are arranged so that their grooves form equilateral triangles. We define the radial unit vectors $\hat{x}$ and $\hat{y}$ to be perpendicular and parallel to the grooves of one of the linear gratings. At $\lambda_{\mathrm{Li}} \approx 671$ nm, each grating has a first-order diffraction efficiency of 37(1) % and its Stokes parameters for normally incident, left-hand circularly polarized light are $Q = 0.16(1)$,

$U = -0.37(1)$, $V = 0.92(1)$, where $Q = 1$ ($Q = -1$) corresponds to p (s) polarization defined relative to the plane of incidence for each linear grating [46]. (Here, and throughout the paper, parenthetical quantities represent the standard error). The input laser beam is normally incident to the grating chip, generating six diffracted laser beams at an angle $\theta_d \approx \pm 42^\circ$ relative to the chip normal $-\hat{z}$. The diffracted beams that propagate toward the center of the quadrupole magnetic field combine with the input beam to produce an irregular-tetrahedral laser beam geometry suitable for magneto-optical trapping or optical molasses [10, 21, 47, 48]. The center of the input laser beam passes through a triangular aperture etched in the grating chip and strikes the Li dispenser. Lithium atoms emitted from the dispenser are Zeeman slowed behind the chip and then captured into the grating MOT after transiting the chip aperture.

Magneto-optical trapping and Λ-enhanced molasses cooling require distinct input laser beams: the cooling beam and molasses beam, respectively. Both beams have a $1/e^2$ radius of approximately 18 mm. An iris truncates the Gaussian spatial mode of both beams at a radius of 11 mm to fit the patterned area of the grating chip. The center frequency of the cooling beam is detuned by Δ_c from the $^2\mathrm{S}_{1/2}\,(F = 2) \rightarrow {}^2\mathrm{P}_{3/2}\,(F' = 3)$ cycling transition. An electro-optic modulator (EOM) frequency modulates the cooling beam at approximately 813 MHz, so the +1st-order sideband is detuned by Δ_c from the $^2\mathrm{S}_{1/2}\,(F = 1) \rightarrow {}^2\mathrm{P}_{3/2}\,(F' = 2)$ "repump" transition. We set the modulation depth of the EOM to produce a $1 : 2$ ratio of the repump intensity to the cooling intensity I_c. The center frequency of the molasses beam is detuned by Δ_2 from the $^2\mathrm{S}_{1/2}\,(F = 2) \rightarrow {}^2\mathrm{P}_{1/2}\,(F' = 2)$ transition. Another EOM, nominally operating at the ^{7}Li ground state hyperfine splitting $\nu_{hfs} \approx 803.5$ MHz, adds sidebands for repumping to the molasses beam and detunes the +1st-order sideband by Δ_1 from the $^2\mathrm{S}_{1/2}\,(F = 1) \rightarrow {}^2\mathrm{P}_{1/2}\,(F' = 2)$ transition. The modulation frequency of the molasses EOM controls the 2-photon Raman detuning $\delta = \Delta_1 - \Delta_2$ of the Λ-system defined by $^2\mathrm{S}_{1/2}\,(F = 1)$, $^2\mathrm{S}_{1/2}\,(F = 2)$, and $^2\mathrm{P}_{1/2}\,(F' = 2)$. The modulation depth of the molasses EOM governs the relative intensity of the molasses carrier I_2 and the molasses sideband I_1. The $^2\mathrm{S}_{1/2} \rightarrow {}^2\mathrm{P}_{3/2}$ cooling transition and the $^2\mathrm{S}_{1/2} \rightarrow {}^2\mathrm{P}_{1/2}$ molasses transition both have natural linewidth $\Gamma_{\mathrm{Li}} \approx 2\pi \times 5.87$ MHz. The saturation intensity of the cooling transition is $I_{\mathrm{sat}} \approx 2.54\ \mathrm{mW\,cm^{-2}}$. The molasses and cooling beams are combined using a polarizing beam cube and a Pockels cell, so both beams are left-hand circularly polarized (σ^-) with respect to the quantization axis $\hat{z}$.

We have implemented three upgrades to the apparatus in Ref. [4]. First, three pairs of magnetic shim coils now surround the vacuum chamber. The shim coils null the ambient magnetic field and are active throughout our experimental sequence. Second, the commercial Li vapor source has been replaced with a lower-outgassing, three-dimensionally printed titanium dispenser [42]. Third, the dispenser is now placed approximately 2 cm behind the nanofabricated grating chip, near the peak magnetic field of the grating MOT's integrated Zeeman slower. Combined with the reduced $1/e^2$ radius of the input cooling beam [4], the latter two upgrades have increased the maximum number of trapped lithium atoms by a factor of 7. The higher trapped atom number increased the signal-to-noise ratio of our resonant absorption imaging, allowing us to observe sub-Doppler cooling.

3. Experiment

We begin our measurements by preparing a cloud of cold ^{7}Li atoms in the grating MOT. To load atoms, we operate the MOT at a nominal axial magnetic field gradient $B' = 6\ \mathrm{mT\,cm^{-1}}$, cooling laser detuning $\Delta_c/\Gamma_{\mathrm{Li}} = -5.1$, and carrier saturation parameter $s_c = I_c/I_{\mathrm{sat}} = 4.9$. The MOT loading stage lasts for 0.65 s, which is similar to the trap lifetime $\tau \approx 0.8$ s. At the end of the loading stage, the grating MOT contains approximately 7×10^6 ^{7}Li atoms at a radial temperature $T_x \approx 2$ mK and an axial temperature $T_z \approx 1$ mK. We then compress the MOT for 2.5 ms by jumping the cooling laser detuning to $\Delta_c/\Gamma_{\mathrm{Li}} = -2.0$ and simultaneously reducing the carrier saturation parameter to $s_c = 0.5$. The compressed grating MOT captures all atoms from the

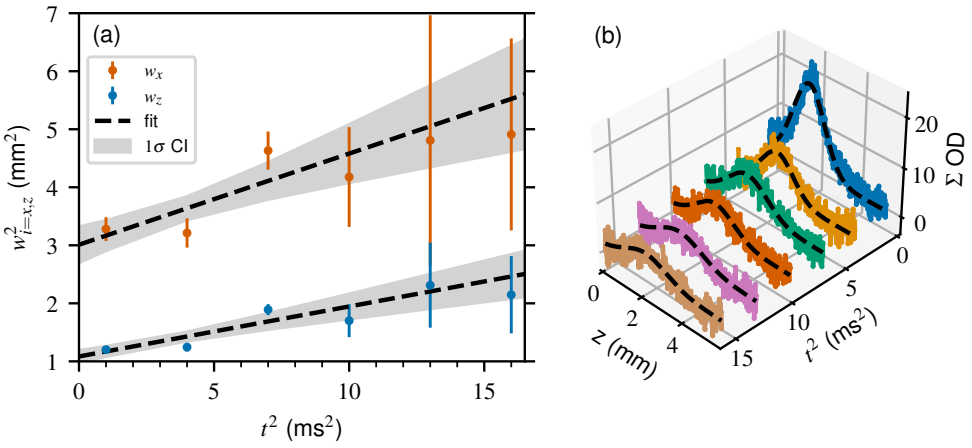

Fig. 1. Example time-of-flight sequence. (a) The x (red) and z (blue) squared $1/e$ radii $w^2_{i=x,z}(t)$ plotted as a function of t^2. Errorbars, some of which are smaller than the data points, denote the standard error. Black dashed lines are fits to Eq. 1 with the associated 1σ confidence interval (CI) shown in gray. For this sequence, $T_x = 66(26)$ μK and $T_z = 36(11)$ μK. (b) Average absorption images integrated over x (colored points) at each time of flight for the sequence in (a). Black dashed lines show integrated 2-dimensional Gaussian fits to the average absorption image.

loading stage and cools them to a radial temperature $T_x \approx 650$ μK and an axial temperature $T_z \approx 350$ μK.

We transfer the atoms from the MOT into the Λ-enhanced gray molasses by extinguishing the cooling beam, turning off the MOT electromagnets, and activating the molasses beam. The nominal parameters of the molasses beam are 1-photon detuning $\Delta_2/\Gamma_{\mathrm{Li}} = 3.1$, 2-photon detuning $\delta/\Gamma_{\mathrm{Li}} = 0$, total saturation $s_m = (I_1 + I_2)/I_{\mathrm{sat}} = 3.2(1)$, and sideband-to-carrier ratio $I_1/I_2 = 0.233(4)$. The momentum distribution of the atom cloud evolves within the gray molasses for 1 ms.

We measure the temperature of the atoms with a time of flight method. After shutting off the molasses beam, we record the distribution of the atom cloud using resonant absorption imaging for a sequence of times of flight t. The absorption images are fit to a 2-dimensional Gaussian to extract the radial and axial $1/e$ widths of the atom cloud $w_x(t)$ and $w_z(t)$, respectively. We repeat the time-of-flight sequence four times and fit the average atom cloud radii to

$$w_i^2(t) = w_i^2(0) + \frac{2k_B T_i}{m} t^2, \tag{1}$$

where k_B is Boltzmann's constant, m is the atomic mass of ^{7}Li, and T_i is the molasses temperature along axis $i = x, z$. Figure 1 shows an example time-of-flight sequence for the nominal molasses operation parameters. Before scanning a molasses parameter, we run a time-of-flight sequence with the nominal parameters to ensure that the shim coils are properly nulling residual magnetic fields.

We study the performance of the Λ-enhanced gray molasses as a function of δ, Δ_2, and I_1/I_2. Figure 2 shows the atom cloud temperatures T_x and T_z, as well as the the molasses capture efficiency, as a function of $\delta/\Gamma_{\mathrm{Li}}$. For the data in Fig. 2, $\Delta_2/\Gamma_{\mathrm{Li}} = 3.1$, $s_m = 3.2(1)$, and $I_1/I_2 = 0.233(4)$. We observe strong sub-Doppler cooling to $T_x = 60(9)$ μK and $T_z = 23(3)$ μK at Raman resonance ($\delta/\Gamma_{\mathrm{Li}} = 0$). The ratios of the final temperatures to the Doppler temperature are $T_x/T_D = 0.43(6)$ and $T_z/T_D = 0.16(2)$, indicating that Λ-enhanced cooling occurs in our

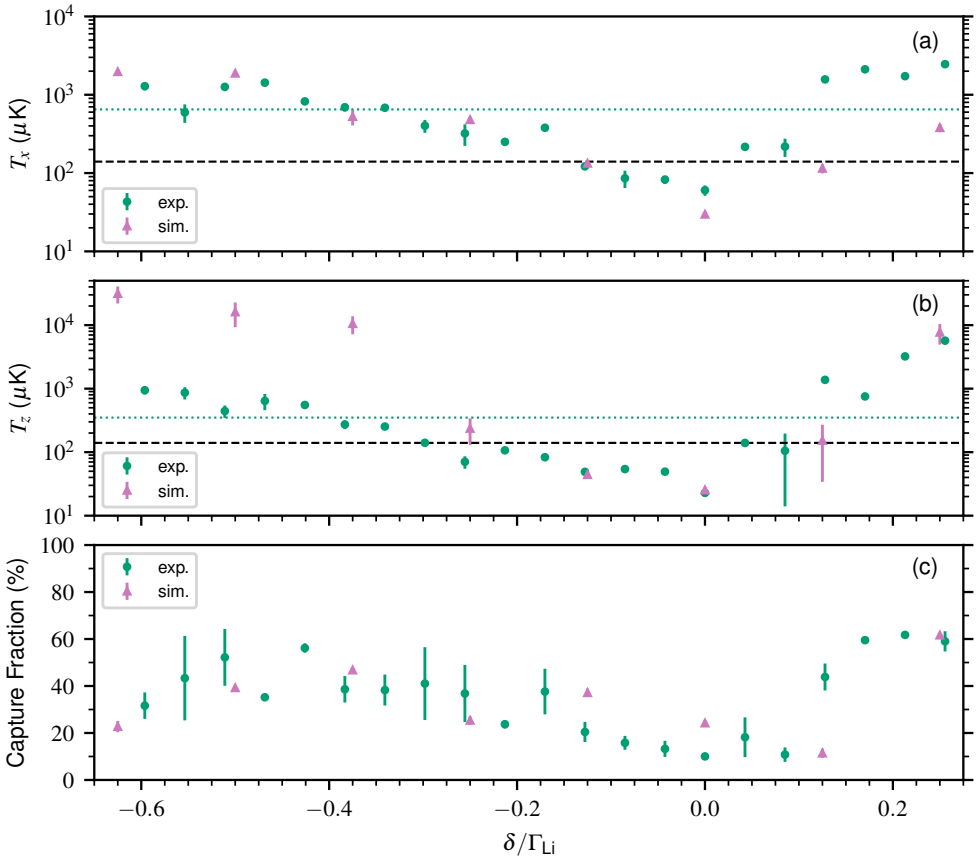

Fig. 2. Λ-enhanced molasses performance as a function of Raman detuning $\delta/\Gamma_{\mathrm{Li}}$. Green circles in (a) and (b) show the measured radial temperature T_x and axial temperature T_z, respectively. The horizontal dotted lines indicate the temperature of the compressed grating MOT and the horizontal dashed lines represent the Doppler cooling limit for lithium. (c) shows the capture efficiency of the Λ-enhanced molasses (green circles). In all three subplots, pink triangles are results of optical Bloch equation simulations of the Λ-enhanced cooling process (see Sec. 4). Errorbars represent the standard error and are often smaller than the data points.

tetrahedral laser beam geometry. Our final temperatures are comparable to the approximately 40 μK temperatures achieved in conventional 6-beam Λ-enhanced molasses configurations with lithium [34, 49–52]. For $\delta/\Gamma_{\mathrm{Li}} > 0$, the Λ-enhanced molasses heats the atom cloud as expected when $I_2 > I_1$ [50]. However, in contrast to prior experiments, we see no evidence of incoherent gray molasses cooling when $\delta/\Gamma_{\mathrm{Li}} < 0$ [33, 34, 49–57]. The fraction of atoms that are captured from our MOT into the molasses stage at Raman resonance is 11(2) %, substantially lower than the greater than 50 % capture efficiency seen in 6-beam lithium experiments using molasses with similar intensity [49–51]. We explore whether the low capture efficiency and lack of incoherent D_1 gray molasses cooling are features of our non-orthogonal molasses beam arrangement, or merely a result of the molasses parameters, in Sec. 4.

Figure 3 shows the change in Λ-enhanced molasses temperature and capture efficiency with Δ_2 and I_1/I_2. We note that, because optical power in the −1st-order molasses beam sideband is wasted, s_m decreases with I_1/I_2 in the right column of Fig. 3. For both data sets in Fig. 3,

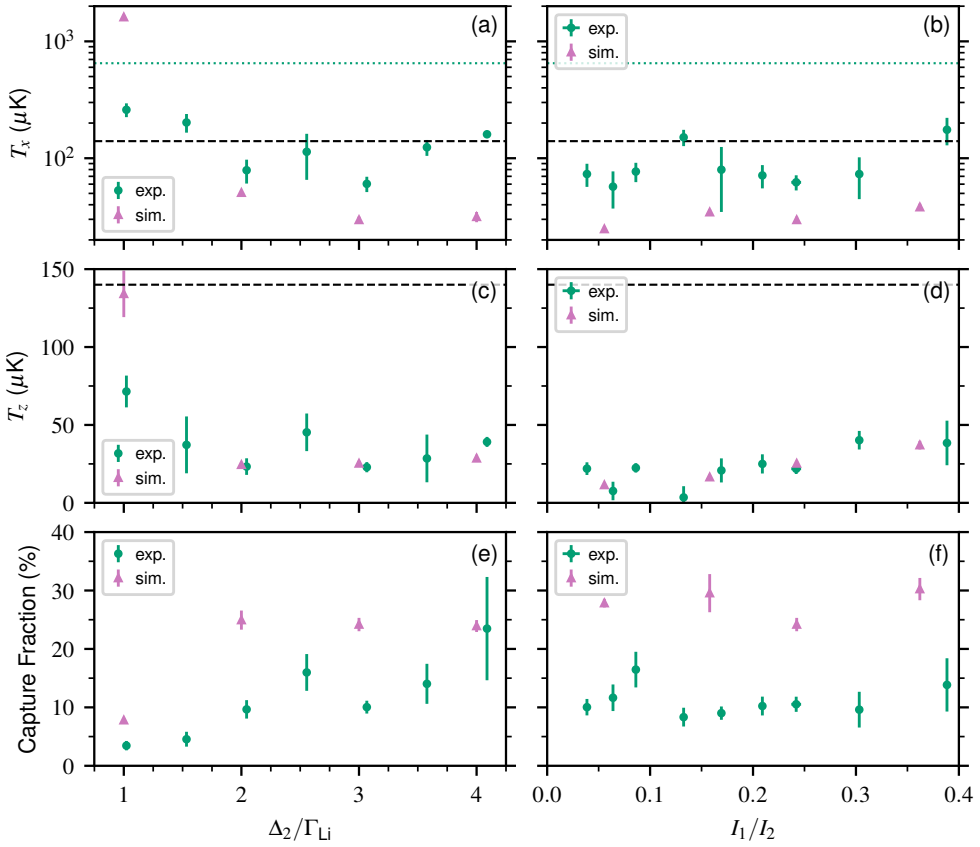

Fig. 3. Λ-enhanced molasses performance as a function of 1-photon detuning Δ_2 and sideband-to-carrier ratio I_1/I_2. (a), (c), (e) show T_x, T_z, and the capture efficiency as a function of Δ_2, respectively. (b), (d), (f) are the corresponding plots of the molasses performance as a function of I_1/I_2. In all six subplots, green circles denote experimental data and pink triangles are results of optical Bloch equation simulations of the Λ-enhanced cooling process (see Sec 4). The horizontal dashed lines in (a), (b), (c), (d) indicate the Doppler cooling limit for lithium. The horizontal dotted lines in (a) and (b) show the temperature of the compressed grating MOT. The experimental data in (a), (c), (e) have $s_m = 3.2(1)$ and $I_1/I_2 = 0.233(4)$, while the data (b), (d), (f) have $\Delta_2/\Gamma_{Li} = 3.1$. In all subplots, errorbars show the standard error.

the Raman detuning $\delta/\Gamma_{Li} = 0$. The radial and axial temperatures increase for $\Delta_2/\Gamma_{Li} < 2.0$ and are flat for $\Delta_2/\Gamma_{Li} \geq 2.0$. Most 6-beam experiments observe a temperature minimum at $\Delta_2/\Gamma \approx 5$ [33,49,51,53,54,56,57]. Our molasses capture efficiency increases with Δ_2, but more slowly than in the 6-beam geometry [33,49–51,56,57]. The axial temperature of the gray molasses increases with I_1/I_2, while the radial temperature and capture efficiency are flat. Our molasses performance as a function of I_1/I_2 is roughly consistent with 6-beam experiments [34,51,54,57], which see a temperature increase and a flat capture efficiency.

4. Simulation

To investigate the lack of incoherent gray molasses and low capture efficiency of the tetrahedral gray molasses (see Fig. 2), we simulate the molasses cooling process using the optical Bloch

equations. Our simulation numerically integrates the classical motion and density matrix evolution of the atom in the optical field of the tetrahedral Λ-enhanced gray molasses for 1 ms. We generate the optical Bloch equations for the Zeeman level structure of $^2S_{1/2}(F = 1)$, $^2S_{1/2}(F = 2)$, and $^2P_{1/2}(F' = 2)$ with our grating laser beam arrangement using the `pylcp` Python package [58]. We program the laser beams with pure circular polarization and uniform intensity profiles [59], but we reduce the intensity of the diffracted beams to account for the Gaussian intensity profile of the input molasses beam projected onto the measured position of the MOT. Each simulated trajectory initializes with an atom at the origin, with a random velocity drawn from a Maxwell-Boltzmann distribution, and a density matrix with equal populations in each of the $^2S_{1/2}$ $(F = 1)$ Zeeman states. The initial density matrix ensures atoms are not initialized in a coherent dark state. The simulation also includes the effects of gravity and random recoil due to spontaneous emission.

Both Λ-enhanced cooling and gray molasses are sub-recoil cooling techniques [28–31]. Because our simulation does not include the effects of secondary scattering, stimulated momentum diffusion, quantum jumps and technical noise, the simulations produce temperatures far lower than our experimental observations. Secondary scattering is insignificant in our experiment because the radial and axial velocity distributions are not in thermal equilibrium (see Fig. 2). The stimulated momentum diffusion rate is not calculated by the `pylcp` package. There is not a closed-form expression for the stimulated diffusion rate as function of velocity and approximations based on two-level atoms are not applicable to our degenerate Λ level structure [18, 58, 60]. Quantum jumps would heat the simulated molasses since they disturb the evolution of the density matrix into a coherent dark state. However, prior Λ-enhanced cooling simulations that included quantum jumps also did not quantitatively reproduce experimentally observed temperatures [50, 61]. We apply a uniform magnetic field $B_z = 40$ μT along the axial direction $\hat{z}$ in our simulations to approximate the effect of technical noise sources (such as residual magnetic field gradients and Raman detuning jitter due to phase noise from the frequency synthesizer driving the molasses EOM) [62]. We chose the value of B_z so the simulated and experimental axial temperature at $\delta/\Gamma_{\mathrm{Li}} = 0$ would match after 200 trajectories.

We integrate 1000 atomic trajectories within the molasses at each of 8 Raman detunings, 4 1-photon detunings, and 4 settings for I_1/I_2. The nominal molasses parameters for the simulated trajectories are $\delta/\Gamma_{\mathrm{Li}} = 0$, $\Delta_2/\Gamma_{\mathrm{Li}} = 3.0$, $s_m = 3.2$, and $I_1/I_2 = 0.24$; chosen to match the experimental conditions for Fig. 2. To increase the number of trajectories that the molasses captures, we sample the initial atomic velocities from an isotropic Maxwell-Boltzmann distribution at the Doppler temperature. We construct a histogram of the final velocities along each axis following a Bayesian approach [63]. Each histogram is fitted with both a unimodal and a bimodal Gaussian distribution to extract the molasses temperature, which is the smaller temperature in the case of the bimodal distribution. To mitigate overfitting, we use the Bayesian information criterion to decide whether the unimodal or bimodal fit best represents the binned trajectories [64–66]. Fig. 4 shows the histogrammed simulation results and Gaussian fits for $\delta/\Gamma_{\mathrm{Li}} = 0$. The asymmetry of the tetrahedral laser arrangement is most apparent in the velocity distribution along $\hat{z}$. To compare with the experimental data, we average the simulated temperatures along $\hat{x}$ and $\hat{y}$ to compute the simulated radial molasses temperature.

The simulations reproduce the main features of the experimental data. Pink triangles show the simulated radial molasses temperature as a function of $\delta/\Gamma_{\mathrm{Li}}$, $\Delta_2/\Gamma_{\mathrm{Li}}$, and I_1/I_2 in Fig. 2(a), Fig. 3(a), and Fig. 3(b), respectively. Pink triangles in Fig. 2(b), Fig. 3(c), and Fig. 3(d) show the corresponding simulation results for the axial molasses temperature. In Fig. 2(a) and Fig. 2(b), the simulations exhibit sub-Doppler cooling when $\delta/\Gamma_{\mathrm{Li}} \approx 0$ and strong heating when $\delta/\Gamma_{\mathrm{Li}} \lesssim -0.25$ or $\delta/\Gamma_{\mathrm{Li}} \gtrsim 0.1$. The simulations also show that the lack of incoherent gray molasses cooling near $\delta/\Gamma_{\mathrm{Li}} \approx -0.5$ is expected for our molasses parameters. Lithium atoms with velocity $v \geq 2.7$ m s^{-1}, corresponding to a thermal energy of $k_B \times 6$ mK, escape the field of view of

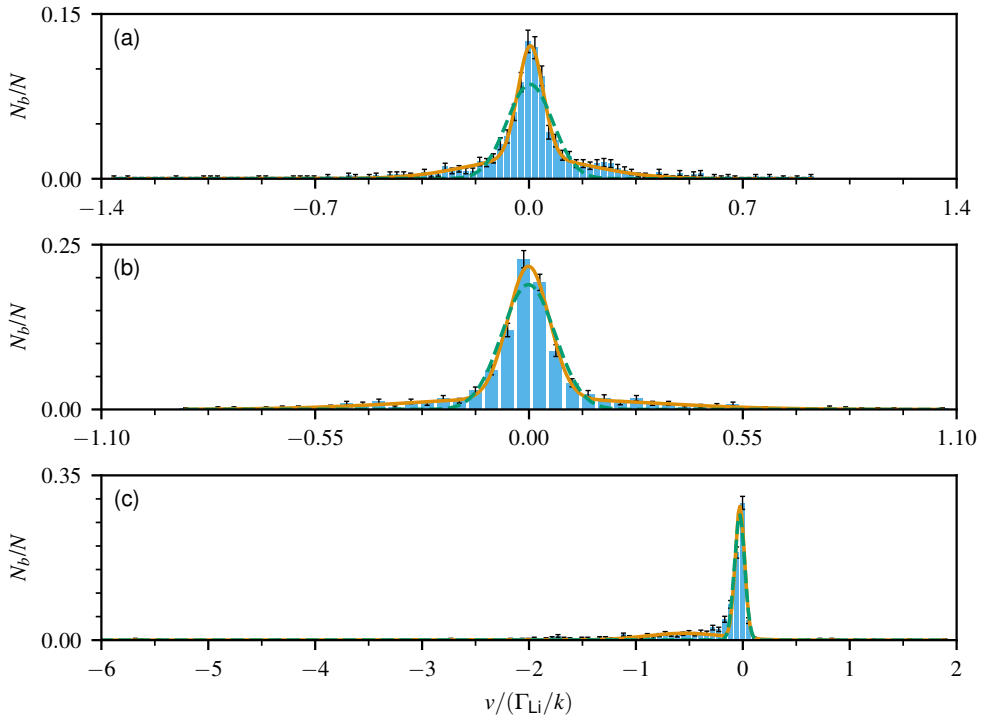

Fig. 4. Example simulated velocity distribution of Λ-enhanced gray molasses in our tetrahedral laser beam geometry. The fraction of atoms in each velocity bin N_b/N (blue pillars) along the x, y, and z axes are shown as a function of velocity v in subplot (a), (b), and (c), respectively. Black errorbars on each pillar are the uncertainty in N_b/N, calculated following Ref. [63]. We fit the velocity distributions along each axis to a unimodal Gaussian distribution (green line) and a bimodal Gaussian distribution (orange line) to extract the temperature. The example velocity distributions were constructed from 1000 simulated molasses cooling trajectories with $\Delta_2/\Gamma_{\mathrm{Li}} = 3.0$, $\delta/\Gamma_{\mathrm{Li}} = 0$, $s_m = 3.2$, and $I_1/I_2 = 0.24$. The wavenumber of the molasses cooling transition is $k = 2\pi/\lambda_{\mathrm{Li}}$.

our imaging system in approximately 1.5 ms, which is the final time-of-flight for the data with $\delta/\Gamma_{\mathrm{Li}} \approx -0.5$ in Fig. 2. The escape of high velocity atoms from the field of view at least partially explains the comparatively large disagreement between the axial simulation and experiment near $\delta/\Gamma_{\mathrm{Li}} \approx -0.5$. In Fig. 3(a) and Fig. 3(c), the simulated molasses temperatures increase when $\Delta_2/\Gamma_{\mathrm{Li}} < 2.0$ and plateau when $\Delta_2/\Gamma_{\mathrm{Li}} \geq 2.0$. The simulated axial molasses temperature increases as a function of I_1/I_2 (see Fig. 3(d)), while the simulated radial temperature is flat (see Fig. 3(b)). The agreement between simulation and experiment in Figs. 3(a), 3(b), 3(c), and 3(d) is better for the axial temperature, but the level of agreement for the radial temperature is comparable to prior 6-beam simulations of Λ-enhanced cooling [50, 61].

We simulate the capture efficiency of the molasses by integrating 200 trajectories with initial velocities sampled from an anisotropic Maxwell-Boltzmann distribution with radial and axial temperatures matching the compressed MOT. Once again, the nominal simulated molasses parameters are similar to the experiment: $\delta/\Gamma_{\mathrm{Li}} = 0$, $\Delta_2/\Gamma_{\mathrm{Li}} = 3.0$, $s_m = 3.2$, and $I_1/I_2 = 0.24$. After 1 ms of integration, we construct empirical cumulative distribution functions (ECDF) for the final velocities along each axis. (Histograms of the final velocities do not reliably extract the

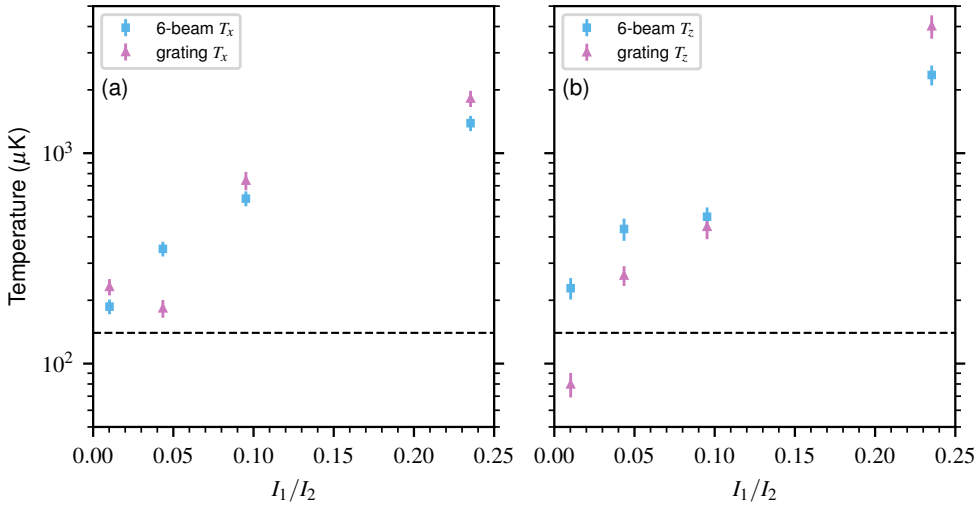

Fig. 5. Simulated temperature of Λ-enhanced gray molasses as a function of I_1/I_2. (a) shows simulated radial temperatures and (b) shows simulated axial temperatures. Pink triangles and blue squares show simulation results for the grating beam configuration and a conventional 6-beam configuration, respectively. The horizontal dashed lines indicate the Doppler cooling limit for lithium. The grating molasses and the 6-beam molasses have the same total intensity. Each temperature was extracted from 200 molasses cooling trajectories with $\Delta_2/\Gamma_{\mathrm{Li}} = 3.0$, $\delta/\Gamma_{\mathrm{Li}} = -0.5$, and $B_z = 0$ μT. At $I_1/I_2 = 0.24$, $s_m = 3.2$. In both subplots, errorbars show the standard error.

sub-Doppler features for this simulation set). Single, double, and triple Gaussian error functions are fit to each ECDF with the Bayesian information criterion determining the best model for the simulated data. The triple error function is only fit to the axial velocities, which are not fully described by a bimodal distribution when the capture efficiency is low. Most simulated trajectories escape the molasses along the axial direction $\hat{z}$, so we compute the simulated molasses capture efficiency using the amplitude of the coldest error function from the fit to the axial velocities. Pink triangles in Fig. 2(c), Fig. 3(e), and Fig. 3(f) show the simulated capture efficiency as a function of $\delta/\Gamma_{\mathrm{Li}}$, $\Delta_2/\Gamma_{\mathrm{Li}}$, and I_1/I_2, respectively. The simulations in Fig. 2(c) predict a higher capture efficiency at Raman resonance, but otherwise agree with the experimental data. In both Fig. 3(e) and Fig. 3(f), the simulated capture efficiencies are substantially higher than our experimental observations, but are still much lower than observations in 6-beam lithium molasses experiments [49–51]. The simulated capture efficiency initially increases with $\Delta_2/\Gamma_{\mathrm{Li}}$, but flattens when $\Delta_2/\Gamma_{\mathrm{Li}} \geq 2.0$. In Fig. 3(f) the simulations follow the trend in the data: the capture efficiency is flat as a function of I_1/I_2. The trajectory set that we initialized at the Doppler temperature had a capture efficiency of approximately 60 % at $\delta/\Gamma_{\mathrm{Li}} = 0$ (see Fig. 4), so the small experimentally observed capture efficiency is not inherent to the tetrahedral laser beam arrangement. The number of atoms in the molasses would be improved with better precooling in the grating MOT or, possibly, by increasing the molasses intensity s_m.

The apparent lack of incoherent gray molasses cooling in the tetrahedral beam geometry is due to our choice of experimental parameters. When $\delta/\Gamma_{\mathrm{Li}} < 0$, atoms in $^2\mathrm{S}_{1/2}\,(F = 1)$ Zeeman states gain kinetic energy whenever they are optically pumped into $^2\mathrm{S}_{1/2}\,(F = 2)$. Gray molasses cooling still occurs because the $^2\mathrm{S}_{1/2}\,(F = 2) \rightarrow {}^2\mathrm{P}_{1/2}\,(F' = 2)$ transition still has a dark state. However, the gray molasses cooling rate only exceeds the heating rate due to $^2\mathrm{S}_{1/2}\,(F = 1) \rightarrow {}^2\mathrm{S}_{1/2}\,(F = 2)$ optical pumping when $I_1 \ll I_2$. Figure 5 shows the simulated

I_1/I_2 dependence of the gray molasses radial and axial temperatures at $\delta/\Gamma_{\mathrm{Li}} = -0.5$. Each temperature was extracted from a Gaussian fit to the binned final velocities of 200 trajectories initialized at the Doppler temperature. To avoid washing out the sub-Doppler feature, $B_z = 0$ μT for this simulation set. The simulations of the grating beam geometry indicate that incoherent molasses temperatures near the Doppler limit are achievable when $I_1/I_2 < 0.05$, comparable to both measurements in 6-beam experiments [34, 52] and our own simulations of 6-beam gray molasses cooling (see Fig. 5).

5. Conclusion

We have demonstrated Λ-enhanced gray molasses cooling in a tetrahedral beam configuration. A single input laser beam striking a nanofabricated grating chip produces the molasses light field. The Λ-enhanced molasses cools ^{7}Li atoms to radial and axial temperatures as low as $T_x = 60(9)$ μK and $T_z = 23(3)$ μK, respectively. The molasses captures 11(2) % of the lithium atoms from a grating MOT. Optical Bloch equation simulations of the Λ-enhanced cooling process adequately reproduce our measured temperature and capture efficiency. The simulations suggest that the capture efficiency of the molasses can be improved by either increasing the molasses intensity or reducing the temperature of the compressed grating MOT. The simulations also indicate that the lack of incoherent gray molasses cooling to the red of Raman resonance is not a feature of the irregular tetrahedral beam geometry, but a consequence of our experimental setting for I_1/I_2. By reducing the amount of molasses repumping light, sub-Doppler temperatures should be attainable at a small red detuning from Raman resonance, which maximizes the gray molasses capture efficiency [49, 51, 57]. Our work demonstrates that sub-Doppler temperatures are attainable in the beam geometries produced by diffraction grating chips, even for atomic species or molecules that are not amenable to bright molasses cooling. The realization of dark-state-based laser cooling with a diffraction grating chip opens new application spaces for grating MOTs, allowing them to serve as atom sources for quantum network nodes [39], primary vacuum gauges [9], and Rydberg-atom quantum computers [25].

Acknowledgments

We thank T. Bui and R. Fasano for their careful reading of the manuscript. We also thank J. Fletcher for assistance assembling the molasses laser system and T. Koch for bringing Ref. [63] to our attention. We acknowledge funding from the National Institute of Standards and Technology.

Disclosures

The authors declare no conflict of interest.

Data Availability

The data underlying the results presented in this paper are not publicly available, but may be obtained from the authors upon reasonable request.

References

1. J. A. Rushton, M. Aldous, and M. D. Himsworth, "Contributed Review: The feasibility of a fully miniaturized magneto-optical trap for portable ultracold quantum technology," Rev. Sci. Instruments **85**, 121501 (2014).
2. M. Keil, O. Amit, S. Zhou, D. Groswasser, Y. Japha, and R. Folman, "Fifteen years of cold matter on the atom chip: promise, realizations, and prospects," J. Mod. Opt. **63**, 1840 (2016).
3. M. Vangeleyn, P. F. Griffin, E. Riis, and A. S. Arnold, "Laser cooling with a single laser beam and a planar diffractor," Opt. Lett. **35**, 3453 (2010).
4. D. S. Barker, E. B. Norrgard, N. N. Klimov, J. A. Fedchak, J. Scherschligt, and S. Eckel, "Single-Beam Zeeman Slower and Magneto-Optical Trap Using a Nanofabricated Grating," Phys. Rev. Appl. **11**, 064023 (2019).
5. R. Elvin, G. W. Hoth, M. Wright, B. Lewis, J. P. McGilligan, A. S. Arnold, P. F. Griffin, and E. Riis, "A cold-atom clock based on a diffractive optic," Opt. Express **27**, 38359 (2019).

6. J. Lee, R. Ding, J. Christensen, R. R. Rosenthal, A. Ison, D. P. Gillund, D. Bossert, K. H. Fuerschbach, W. Kindel, P. S. Finnegan, J. R. Wendt, M. Gehl, H. McGuinness, C. A. Walker, A. Lentine, S. A. Kemme, G. Biedermann, and P. D. D. Schwindt, "A Cold-Atom Interferometer with Microfabricated Gratings and a Single Seed Laser," ArXiv:2107.04792 (2021).
7. J. G. H. Franssen, T. C. H. de Raadt, M. A. W. van Ninhuijs, and O. J. Luiten, "Compact ultracold electron source based on a grating magneto optical trap," Phys. Rev. Accel. Beams **22**, 023401 (2019).
8. J. P. McGilligan, P. F. Griffin, R. Elvin, S. J. Ingleby, E. Riis, and A. S. Arnold, "Grating chips for quantum technologies," Sci. Reports **7**, 384 (2017).
9. S. Eckel, D. S. Barker, J. A. Fedchak, N. N. Klimov, E. Norrgard, J. Scherschligt, C. Makrides, and E. Tiesinga, "Challenges to miniaturizing cold atom technology for deployable vacuum metrology," Metrologia **55**, S182 (2018).
10. C. C. Nshii, M. Vangeleyn, J. P. Cotter, P. F. Griffin, E. A. Hinds, C. N. Ironside, P. See, A. G. Sinclair, E. Riis, and A. S. Arnold, "A surface-patterned chip as a strong source of ultracold atoms for quantum technologies," Nat. Nanotechnol. **8**, 321 (2013).
11. J. P. Cotter, J. P. McGilligan, P. F. Griffin, I. M. Rabey, K. Docherty, E. Riis, A. S. Arnold, and E. A. Hinds, "Design and fabrication of diffractive atom chips for laser cooling and trapping," Appl. Phys. B **122**, 172 (2016).
12. W. R. McGehee, W. Zhu, D. S. Barker, D. Westly, A. Yulaev, N. Klimov, A. Agrawal, S. Eckel, V. Aksyuk, and J. J. McClelland, "Magneto-optical trapping using planar optics," New J. Phys. **23**, 013021 (2021).
13. J. P. McGilligan, K. R. Moore, A. Dellis, G. D. Martinez, E. De Clercq, P. F. Griffin, A. S. Arnold, E. Riis, R. Boudot, and J. Kitching, "Laser cooling in a chip-scale platform," Appl. Phys. Lett. **117**, 054001 (2020).
14. O. S. Burrow, P. F. Osborn, E. Boughton, F. Mirando, D. P. Burt, A. S. Arnold, P. F. Griffin, and E. Riis, "A centilitre-scale vacuum chamber for compact ultracold quantum technologies," ArXiv:2101.07851 (2021).
15. E. L. Raab, M. Prentiss, A. Cable, S. Chu, and D. E. Pritchard, "Trapping of Neutral Sodium Atoms with Radiation Pressure," Phys. Rev. Lett. **59**, 2631 (1987).
16. J. P. McGilligan, P. F. Griffin, E. Riis, and A. S. Arnold, "Phase-space properties of magneto-optical traps utilising micro-fabricated gratings," Opt. Express **23**, 8948 (2015).
17. E. Imhof, B. K. Stuhl, B. Kasch, B. Kroese, S. E. Olson, and M. B. Squires, "Two-dimensional grating magneto-optical trap," Phys. Rev. A **96**, 033636 (2017).
18. P. J. Ungar, D. S. Weiss, E. Riis, and S. Chu, "Optical molasses and multilevel atoms: theory," J. Opt. Soc. Am. B **6**, 2058 (1989).
19. P. D. Lett, W. D. Phillips, S. L. Rolston, C. E. Tanner, R. N. Watts, and C. I. Westbrook, "Optical molasses," J. Opt. Soc. Am. B **6**, 2084 (1989).
20. K. I. Petsas, A. B. Coates, and G. Grynberg, "Crystallography of optical lattices," Phys. Rev. A **50**, 5173 (1994).
21. J. Lee, J. A. Grover, L. A. Orozco, and S. L. Rolston, "Sub-Doppler cooling of neutral atoms in a grating magneto-optical trap," J. Opt. Soc. Am. B **30**, 2869 (2013).
22. D. Boiron, C. Triché, D. R. Meacher, P. Verkerk, and G. Grynberg, "Three-dimensional cooling of cesium atoms in four-beam gray optical molasses," Phys. Rev. A **52**, R3425 (1995).
23. M. Hauth, C. Freier, V. Schkolnik, A. Senger, M. Schmidt, and A. Peters, "First gravity measurements using the mobile atom interferometer GAIN," Appl. Phys. B **113**, 49 (2013).
24. X. Wu, F. Zi, J. Dudley, R. J. Bilotta, P. Canoza, and H. Müller, "Multiaxis atom interferometry with a single diode laser and a pyramidal magneto-optical trap," Optica **4**, 1545 (2017).
25. M. O. Brown, T. Thiele, C. Kiehl, T. W. Hsu, and C. A. Regal, "Gray-Molasses Optical-Tweezer Loading: Controlling Collisions for Scaling Atom-Array Assembly," Phys. Rev. X **9**, 011057 (2019).
26. A. Sitaram, P. K. Elgee, G. K. Campbell, N. N. Klimov, S. Eckel, and D. S. Barker, "Confinement of an alkaline-earth element in a grating magneto-optical trap," Rev. Sci. Instruments **91**, 103202 (2020).
27. C. Valentin, M. C. Gagné, J. Yu, and P. Pillet, "One-dimension sub-doppler molasses in the presence of static magnetic field," EPL (Europhysics Lett. **17**, 133 (1992).
28. G. Grynberg and J.-Y. Courtois, "Proposal for a magneto-optical lattice for trapping atoms in nearly-dark states," EPL (Europhysics Lett. **27**, 41 (1994).
29. M. S. Shahriar, P. R. Hemmer, M. G. Prentiss, P. Marte, J. Mervis, D. P. Katz, N. P. Bigelow, and T. Cai, "Continuous polarization-gradient precooling-assisted velocity-selective coherent population trapping," Phys. Rev. A **48**, R4035 (1993).
30. P. Marte, R. Dum, R. Taïeb, P. Zoller, M. S. Shahriar, and M. Prentiss, "Polarization-gradient-assisted subrecoil cooling: Quantum calculations in one dimension," Phys. Rev. A **49**, 4826 (1994).
31. M. Weidemüller, T. Esslinger, M. A. Ol'shanii, A. Hemmerich, and T. W. Hänsch, "A Novel Scheme for Efficient Cooling below the Photon Recoil Limit," Europhys. Lett. **27**, 109 (1994).
32. A. Aspect, E. Arimondo, R. Kaiser, N. Vansteenkiste, and C. Cohen-Tannoudji, "Laser Cooling below the One-Photon Recoil Energy by Velocity-Selective Coherent Population Trapping," Phys. Rev. Lett. **61**, 826 (1988).
33. D. R. Fernandes, F. Sievers, N. Kretzschmar, S. Wu, C. Salomon, and F. Chevy, "Sub-Doppler laser cooling of fermionic 40 K atoms in three-dimensional gray optical molasses," EPL (Europhysics Lett. **100**, 63001 (2012).
34. A. T. Grier, I. Ferrier-Barbut, B. S. Rem, M. Delehaye, L. Khaykovich, F. Chevy, and C. Salomon, "Λ-enhanced sub-Doppler cooling of lithium atoms in D_1 gray molasses," Phys. Rev. A **87**, 063411 (2013).
35. S. Truppe, H. J. Williams, M. Hambach, L. Caldwell, N. J. Fitch, E. A. Hinds, B. E. Sauer, and M. R. Tarbutt, "Molecules cooled below the Doppler limit," Nat. Phys. **13**, 1173 (2017).

36. L. Anderegg, B. L. Augenbraun, Y. Bao, S. Burchesky, L. Cheuk, W. Ketterle, and J. M. Doyle, "Laser cooling of optically trapped molecules," Nat. Phys. **14**, 890 (2018).
37. D. J. McCarron, M. H. Steinecker, Y. Zhu, and D. Demille, "Magnetic Trapping of an Ultracold Gas of Polar Molecules," Phys. Rev. Lett. **121**, 013202 (2018).
38. S. Rosi, A. Burchianti, S. Conclave, D. S. Naik, G. Roati, C. Fort, and F. Minardi, "Λ-enhanced grey molasses on the D_2 transition of Rubidium-87 atoms," Sci. Reports **8**, 1301 (2018).
39. D. P. Ornelas-Huerta, A. N. Craddock, E. A. Goldschmidt, A. J. Hachtel, Y. Wang, P. Bienias, A. V. Gorshkov, S. L. Rolston, and J. V. Porto, "On-demand indistinguishable single photons from an efficient and pure source based on a Rydberg ensemble," Optica **7**, 813 (2020).
40. T. Grünzweig, A. Hilliard, M. McGovern, and M. F. Andersen, "Near-deterministic preparation of a single atom in an optical microtrap," Nat. Phys. **6**, 951 (2010).
41. P. T. Starkey, C. J. Billington, S. P. Johnstone, M. Jasperse, K. Helmerson, L. D. Turner, and R. P. Anderson, "A scripted control system for autonomous hardware-timed experiments," Rev. Sci. Instruments **84**, 085111 (2013).
42. E. B. Norrgard, D. S. Barker, J. A. Fedchak, N. Klimov, J. Scherschligt, and S. P. Eckel, "Note: A 3D-printed alkali metal dispenser," Rev. Sci. Instruments **89**, 056101 (2018).
43. J. A. Fedchak, J. Scherschligt, D. Barker, S. Eckel, A. P. Farrell, and M. Sefa, "Vacuum furnace for degassing stainless-steel vacuum components," J. Vac. Sci. Technol. A **36**, 023201 (2018).
44. D. S. Barker, N. C. Pisenti, A. Restelli, J. Scherschligt, J. A. Fedchak, G. K. Campbell, and S. Eckel, "A flexible, open-source radio-frequency driver for acousto-optic and electro-optic devices," arXiv:1908.02156 (2019).
45. W. D. Phillips and H. Metcalf, "Laser deceleration of an atomic beam," Phys. Rev. Lett. **48**, 596 (1982).
46. We use the same grating chip as Ref. [4], but we have corrected the normalization of the Stokes parameters and the sign of V.
47. F. Shimizu, K. Shimizu, and H. Takuma, "Four-beam laser trap of neutral atoms," Opt. Lett. **16**, 339 (1991).
48. Z. Lin, K. Shimizu, M. Zhan, F. Shimizu, and H. Takuma, "Laser Cooling and Trapping of Li," Jpn. J. Appl. Phys. **30**, L 1324 (1991).
49. A. Burchianti, G. Valtolina, J. A. Seman, E. Pace, M. De Pas, M. Inguscio, M. Zaccanti, and G. Roati, "Efficient all-optical production of large ^{6}Li quantum gases using D_1 gray-molasses cooling," Phys. Rev. A **90**, 043408 (2014).
50. F. Sievers, N. Kretzschmar, D. R. Fernandes, D. Suchet, M. Rabinovic, S. Wu, C. V. Parker, L. Khaykovich, C. Salomon, and F. Chevy, "Simultaneous sub-Doppler laser cooling of fermionic ^{6}Li and ^{40}K on the D_1 line: Theory and experiment," Phys. Rev. A **91**, 023426 (2015).
51. C. L. Satter, S. Tan, and K. Dieckmann, "Comparison of an efficient implementation of gray molasses to narrow-line cooling for the all-optical production of a lithium quantum gas," Phys. Rev. A **98**, 023422 (2018).
52. K. Kim, S. Huh, K. Kwon, and J. Choi, "Rapid production of large ^{7}Li Bose-Einstein condensates using D_1 gray molasses," Phys. Rev. A **99**, 053604 (2019).
53. G. Salomon, L. Fouché, P. Wang, A. Aspect, P. Bouyer, and T. Bourdel, "Gray-molasses cooling of 39K to a high phase-space density," EPL (Europhysics Lett. **104**, 63002 (2013).
54. D. Nath, R. K. Easwaran, G. Rajalakshmi, and C. S. Unnikrishnan, "Quantum-interference-enhanced deep sub-Doppler cooling of ^{39}K atoms in gray molasses," Phys. Rev. A **88**, 053407 (2013).
55. Q. Bouton, R. Chang, A. L. Hoendervanger, F. Nogrette, A. Aspect, C. I. Westbrook, and D. Clément, "Fast production of Bose-Einstein condensates of metastable helium," Phys. Rev. A **91**, 061402(R) (2015).
56. H.-Z. Chen, X.-C. Yao, Y.-P. Wu, X.-P. Liu, X.-Q. Wang, Y. X. Wang, Y.-A. Chen, and J.-W. Pan, "Production of large ^{41}K Bose-Einstein condensates using D_1 gray molasses," Phys. Rev. A **94**, 033408 (2016).
57. G. Colzi, G. Durastante, E. Fava, S. Serafini, G. Lamporesi, and G. Ferrari, "Sub-Doppler cooling of sodium atoms in gray molasses," Phys. Rev. A **93**, 023421 (2016).
58. S. Eckel, D. S. Barker, E. B. Norrgard, and J. Scherschligt, "PyLCP: A python package for computing laser cooling physics," ArXiv:2011.07979 (2020).
59. We expect that the effect of polarization impurity due to the grating Stokes parameters is small compared to the effect of projecting the polarization on to the quantization axis $\hat{z}$.
60. A. Ashkin and J. P. Gordon, "Motion of atoms in a radiation trap," Phys. Rev. A **21**, 1606 (1980).
61. G. D. Bruce, E. Haller, B. Peaudecerf, D. A. Cotta, M. Andia, S. Wu, M. Y. H. Johnson, B. W. Lovett, and S. Kuhr, "Sub-Doppler laser cooling of ^{40}K with Raman gray molasses on the D_2 line," J. Phys. B: At. Mol. Opt. Phys. **50**, 095002 (2017).
62. We have also checked that applying the magnetic field along a radial axis or modelling the Raman detuning jitter as a Gaussian-distributed random process produces similar simulation results.
63. K. H. Knuth, "Optimal data-based binning for histograms and histogram-based probability density models," Digit. Signal Process. **95**, 102581 (2019).
64. K. E. Kass and A. E. Raftery, "Bayes Factors," J. Am. Stat. Assoc. **90**, 773 (1995).
65. K. P. Burnham and D. R. Anderson, "Multimodel inference: Understanding AIC and BIC in model selection," Sociol. Methods Res. **33**, 261 (2004).
66. We use the Bayesian information criterion, rather than alternative model selectors like χ^2 or the Akaike information criterion, because it imposes the largest penalty on models with more free parameters.